ACS APPLIED ENERGY MATERIALS

www.acsaem.org Article

Carbon Nanotube/MXene Composite with a Dense Regular Connective Tissue Structure and Its Application in Lithium-Ion Batteries

Zixin Hong, Hui Tian, Zhenhan Fang, Hengcai Wu, Fei Zhao, Qunqing Li, Shoushan Fan, Jiaping Wang,* and Peng Liu*

Cite This: ACS Appl. Energy Mater. 2024, 7, 8004−8013 Read Online

ACCESS | Metrics & More | Article Recommendations | Supporting Information

ABSTRACT: MXene materials hold promise for lithium-ion battery applications but face challenges from interlayer restacking, which impedes both mechanical robustness and ionic transport. Inspired by the dense regular connective tissue of vertebrates, a biomimetic composite is developed, integrating superaligned carbon nanotubes (SACNTs) and Ti_3C_2. In this architecture, SACNTs "fibers" serve as mechanical skeletons and transport channels, while Ti_3C_2 "cells" disperse uniformly and expose abundant lithium storage sites. This composite could endure strains up to 8.01% and 1000 cycles of large-angle bending. Electrochemically, it exhibits commendable rate capabilities (253.1 mA h g^{-1} at 10 A g^{-1}) and robust cycling stability (3300 cycles at 5 A g^{-1}) at room temperature, with sustained functionality even at −40 °C. Density functional theory calculations highlight the efficacy of carbon layers in reducing the adsorption energy toward Li. This biomimetic strategy effectively addresses the challenge of MXene restacking and improves the utility in advanced energy storage.

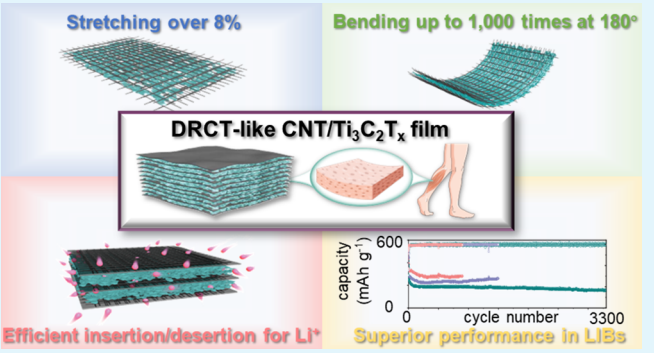

KEYWORDS: *MXene, carbon nanotubes, lithium-ion batteries, biomimetic, flexible device*

1. INTRODUCTION

MXene materials, as emerging luminaries in the realm of two-dimensional materials, have captured widespread interest for their unique architecture and novel properties.[1] They have demonstrated immense potential across various fields, including energy storage, catalysis, medicine, optics, sensing, and electromagnetic shielding.[2] Nevertheless, influenced by van der Waals forces, MXene materials are susceptible to undesirable stacking,[3] which severely hinders their practical application. Taking Ti_3C_2, a representative of MXene, as an example, it indeed exhibits potential in the realm of lithium-ion batteries (LIBs).[4] Compared to commonly used graphite and $Li_4Ti_5O_{12}$ anode materials in LIBs, Ti_3C_2 boasts a low lithium-ion migration barrier (0.07 eV)[5] and remarkable electrical conductivity (10^3−10^4 S cm^{-1}),[6−8] showing potential as a novel anode material upon further maturation of the technology and reduction in production costs (Table 1). However, interlayer stacking results in underutilization of the surface area of Ti_3C_2 (Figure 1a), reducing active sites for ions and degrading the electrochemical performance. Furthermore, the mechanical properties of MXene are also poor, making it difficult to meet the increasing demand for flexible electronic devices, such as smart wristbands, electronic skins, and wearable medical devices.

Table 1. Comparison of Anode Materials[5−12]

	Ti_3C_2	graphite	$Li_4Ti_5O_{12}$
theoretical specific capacity (mA h g^{-1})	320	372	175
Li^+ energy barrier (eV)	0.07	>0.3	>0.3
conductivity (S cm^{-1})	10^3−10^4	10	10^{-10}
cost	high	low	high
maturity of production processes	low	high	high

Various approaches have been proposed to suppress the stacking in MXene materials, such as template method,[13,14] assembly,[15] electrospinning,[16] 3D printing,[17] and freeze-drying.[18] Despite these efforts, the mechanical properties of MXene require further improvement. Combining carbon

Received: July 3, 2024
Revised: August 15, 2024
Accepted: August 22, 2024
Published: August 29, 2024

https://doi.org/10.1021/acsaem.4c01650
ACS Appl. Energy Mater. 2024, 7, 8004−8013

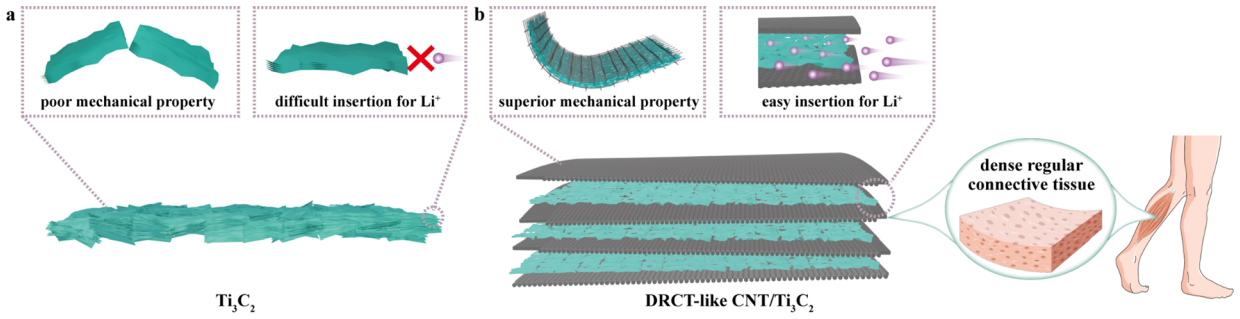

Figure 1. Comparative schematic of Ti_3C_2 and DRCT-like CNT/Ti_3C_2 films. (a) Stacked Ti_3C_2 film with poor mechanical property and challenging lithium-ion intercalation. (b) DRCT-like CNT/Ti_3C_2 films with superior mechanical property and facile lithium-ion insertion.

nanotubes (CNTs) with MXene has emerged as a promising strategy to alleviate stacking and simultaneously improve the mechanical properties of the composite.[19,20] For example, recently Alei Dang et al. prepared a variety of flexible composite electrodes containing MXene and CNT by layer-by-layer method,[21] wet spinning,[22] electrostatic self-assembly, and hydrothermal method[23] capable of achieving 3000−8000 stable cycles. Additionally, given the superior thermal and electrical properties of CNTs, they are anticipated to boost the performance of the composites under extreme temperature conditions. The integration of MXene and CNTs can be categorized into nonreactive and reactive processes.[24] Nonreactive processes encompass physical blending techniques, such as mechanical mixing,[25] self-assembly,[26] codispersion,[27] and electrophoretic deposition.[28] Although these procedures are straightforward, they may necessitate surfactants and introduce impurities. On the other hand, reactive processes involve chemical reactions, such as CVD,[29] thermal treatments,[30] microwave-assisted processes,[31] and hydrothermal methods.[32] These methods could enhance the uniformity of the composite, yet they come with the trade-offs of complex preparation procedures and the potential oxidation of MXenes at elevated temperatures. Typically, these processes result in composites with randomly distributed CNTs and MXene that fail to fully leverage their structural advantages. For instance, electrodes were prepared by sonication and filtration of a mixed dispersion of MXene and CNTs, in which CNTs were distributed in a disordered way.[33−35] Consequently, there is a need to devise novel composite structures of MXene and CNTs, along with a simple, surfactant-free, and room-temperature fabrication process.

Drawing insights from nature offers innovative solutions for addressing contemporary challenges in materials science. Dense regular connective tissue (DRCT) is a fundamental tissue in vertebrates composed of cells, fibers, and ground substances. Cells are functional components, and fibers are arranged around them to provide support, elasticity, and transport channels. Cells and fibers form an ordered and robust structure. Inspired by this configuration, it is natural to design such a similar ordered and robust structure to exhibit the excellent properties of MXene and CNTs. The superaligned CNT (SACNT) is a kind of CNT form with a highly ordered structure and distribution. The SACNTs prepared in previous work feature pristine walls, orderly alignment, and robust intertubular van der Waals forces,[36] enabling the formation of macroscopically ordered structures including one-dimensional fibers, two-dimensional films, and three-dimensional aerogels.[37−40] A biomimetic strategy is proposed to design a DRCT-like structure with SACNTs and Ti_3C_2 for LIBs (Figure 1b). Within this DRCT-like architecture, SACNTs are similar to "fibers", affording mechanical support and promoting the transport of ions and electrons. The Ti_3C_2 "cells" are anticipated to disperse uniformly, exposing abundant accessible sites and enhancing the lithium storage capacity.

Here, we designed a DRCT-like CNT/Ti_3C_2 composite for application as an anode in LIBs. We extracted striped SACNT membranes from the array and integrated them with Ti_3C_2 through an alternate filtration process. Benefiting from this biomimetic structure, the DRCT-like CNT/Ti_3C_2 film could endure a mechanical strain of up to 8.01% and withstand 1000 cycles of extensive bending at angles of 90° and 180°. At room temperature, this anode delivered a specific capacity of 253.1 mA h g^{-1} at a high current density of 10 A g^{-1}, and maintained a considerable capacity even after 3300 stable cycles at 5 A g^{-1}. Impressively, when subjected to a severe temperature of −40 °C, the DRCT-like CNT/Ti_3C_2 anode still retained a substantial specific capacity. To the best of our knowledge, this study represents the first exploration of using MXene as an anode for LIBs at −40 °C. Density functional theory (DFT) calculations revealed that the incorporation of a carbon layer markedly reduced the adsorption energy for Li. This strategy offers a simple and versatile approach to mitigate the stacking predicament inherent in two-dimensional materials, enabling the fabrication of composite materials with superior mechanical and electrochemical properties, and holding promise for application in flexible electronics.

2. EXPERIMENTAL SECTION

2.1. Preparation of SACNTs. The SACNT array was synthesized through an atmospheric-pressure chemical vapor deposition (APCVD) process, following established procedures.[36,37,41] Initially, a silicon dioxide (SiO_2)/silicon (Si) wafer, coated with a thin electron beam-evaporated iron film, was positioned within a semiopen quartz boat. Afterward, controlled heating was applied to the wafer under an argon atmosphere, with temperatures ranging from 660 to 680 °C for 15 min. A precise mixture of hydrogen and acetylene was introduced into the system to catalyze the growth of SACNTs. The resulting SACNTs exhibited dimensions of 8 nm in diameter and 300 μm in height, with clean walls, orderly alignment, and strong intertubular van der Waals forces.

2.2. Preparation of a Striped SACNT Membrane. A monolayer CNT film was carefully extracted from the SACNT array by using a glass rod and placed onto an aluminum frame (side length: 7 cm). Following this, the aluminum frame was rotated 90°, and another monolayer CNT film was similarly extracted and stacked on top of it. By repetition of these steps, a striped SACNT membrane with varying numbers of layers was obtained. These striped SACNT membranes are lightweight (1.5 μg cm^{-2} for a monolayer film),[37] flexible, and capable of withstanding stretching and bending deformations.

https://doi.org/10.1021/acsaem.4c01650
ACS Appl. Energy Mater. 2024, 7, 8004−8013

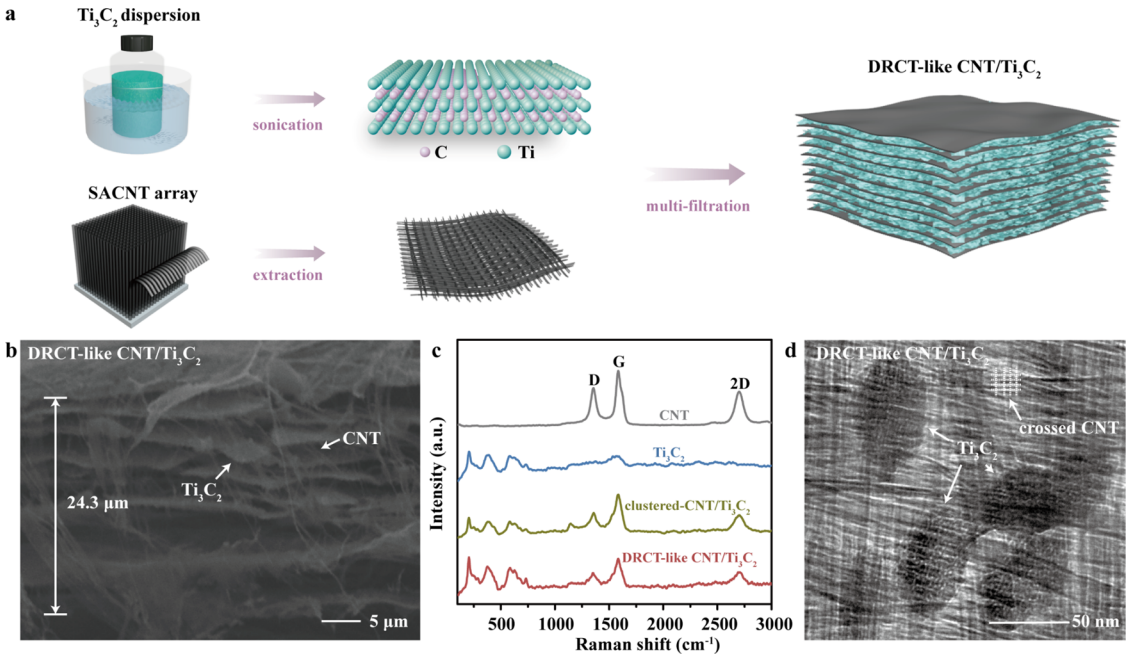

Figure 2. Preparation and characterization of various films. (a) Schematic of the preparation process of the DRCT-like CNT/Ti_3C_2 film. (b) Cross-sectional SEM image of the DRCT-like CNT/Ti_3C_2 film. (c) Raman spectroscopy. (d) TEM image of a portion of the DRCT-like CNT/Ti_3C_2 film.

2.3. Preparation of a Ti_3C_2 Film. 2 mL portion of aqueous dispersion of Ti_3C_2 (5 mg mL^{-1}, 11 Technology Co., Ltd., China) was mixed with 18 mL of deionized water and subjected to ultrasonic treatment at 40 kHz power for 15 min. The resulting Ti_3C_2 solution was employed for the subsequent preparation of various filtration films (aqueous filter membrane with a diameter of 38 mm), with a Ti_3C_2 loading of approximately 0.88 mg cm^{-2}. The Ti_3C_2 solution was directly vacuum filtered to obtain the Ti_3C_2 film.

2.4. Preparation of a Clustered-CNT/Ti_3C_2 Film. The Ti_3C_2 solution was mixed with 1 mg of SACNT and sonicated for 20 min at 10% power using a cell pulverizer (SCIENTZ-IID, SCIENTZ, China). After that, the mixed solution was vacuum filtered, and the collected film was named the clustered-CNT/Ti_3C_2 film. The mass ratio of the CNT within the entire electrode was approximately 9%.

2.5. Preparation of a DRCT-like CNT/Ti_3C_2 Film. The Ti_3C_2 solution was divided into 10 equal portions, each containing 2 mL. Next, ten 4-layer striped SACNT membranes and one 10-layer striped SACNT membranes were prepared. During vacuum filtration, the 10-layer striped SACNT membrane was first laid on the aqueous filter membrane. Then, 2 mL of the Ti_3C_2 solution was vacuum filtered, followed by the addition of a 4-layer striped SACNT membrane. This process was repeated ten times. The resulting film was named DRCT-like CNT/Ti_3C_2-10 (referred to as DRCT-like CNT/Ti_3C_2). In addition, while maintaining the same Ti_3C_2 loading, the layer number of Ti_3C_2 and the striped SACNT membrane was adjusted. The 20 mL portion of Ti_3C_2 solution was divided into 2 and 20 equal portions, respectively. A 10-layer striped SACNT membrane was placed on the filter membrane first, and 4-layer striped SACNT membranes were used in all subsequent filtration processes. The alternating filtration process of Ti_3C_2 dispersion and striped SACNT membrane was repeated 2 and 20 times, and the obtained films were named DRCT-like CNT/Ti_3C_2-2 and DRCT-like CNT/Ti_3C_2-20, accordingly. For DRCT-like CNT/Ti_3C_2-2, DRCT-like CNT/Ti_3C_2-10, and DRCT-like CNT/Ti_3C_2-20, the mass ratios of CNT in the entire electrode were approximately 3, 8, and 13%, respectively.

2.6. Material Analysis. The microstructures were examined through a scanning electron microscope (SEM) (Sirion 200, FEI), a transmission electron microscope (TEM) (Tecnai G2F20, FEI) and the energy dispersive spectroscopy (EDS). To observe cross-sectional SEM images, the samples were immersed in liquid nitrogen and then fractured, resulting in the smoothest possible surface and minimizing deformations introduced during sample preparation. The crystal structure was analyzed in the angular span of 5° to 80° by X-ray diffraction (XRD) employing Cu Kα radiation (Rigaku). Raman spectroscopy was performed with a Raman spectrometer (LabRam-HR/VV, JY) based on a 514 nm He−Ne laser.

2.7. Mechanical Testing. The 50-layer striped SACNT, Ti_3C_2, clustered-CNT/Ti_3C_2, and DRCT-like CNT/Ti_3C_2 were cut into pieces (0.5 × 2 cm). Testing paper was clamped on both sides, leaving an exposed effective length of 1 cm. Tensile tests were conducted at a strain rate of 1% min^{-1} using an Instron 5848 microtiter. For single-cycle bending tests, Ti_3C_2 and DRCT-like CNT/Ti_3C_2 were bent using tweezers, and their postbending morphology was observed under both optical and SEMs. For long-term bending tests, the DRCT-like CNT/Ti_3C_2 was cut into strips (2 cm × 6 cm). The edges of the strips were connected to data collector wires by using conductive silver glue. The bending endurance test was carried out using a bending lifespan tester (LANWAN Precision Instruments Co., Ltd.) with angles ranging from 0° to 90° and 0° to 180°. During the bending process, a rod with a diameter of approximately 1 cm was placed above the sample to limit the bending curvature. The resistance of the sample was recorded in real time by using KE 2400S software.

2.8. Cell Assembly. All battery assembly procedures were performed within an argon glovebox (M. Braun Inert Gas System Co. Ltd., Germany). The films, including 50-layer striped SACNT, Ti_3C_2, clustered-CNT/Ti_3C_2, and DRCT-like CNT/Ti_3C_2, were cut into square pieces with a side length of 5 mm and used as the anode. A lithium sheet served as the cathode, and a commercial PP film was employed as the separator. The electrolyte was 1 M $LiPF_6$ in EC:DMC:EMC = 1:1:1 (vol %).

2.9. Electrochemical Measurement. Cyclic voltammetry (CV) and electrochemical impedance spectroscopy (EIS) were conducted using an electrochemical workstation (EG&G Princeton Applied Research 273A). For CV, the voltage range was set from 0.01 to 3 V, and the scan rates were varied from 0.2, 0.4, 0.6, 0.8, and 1 mV s^{-1}. For EIS, the AC amplitude was 2 mV, and the frequency range was 100 mHz to 100 kHz. GITT was executed with a Land battery system (Wuhan Land Electronic Co., China). This technique involved a sequence of pulsed currents: 10 min at a current density of 0.1 A g^{-1},

https://doi.org/10.1021/acsaem.4c01650
ACS Appl. Energy Mater. 2024, 7, 8004−8013

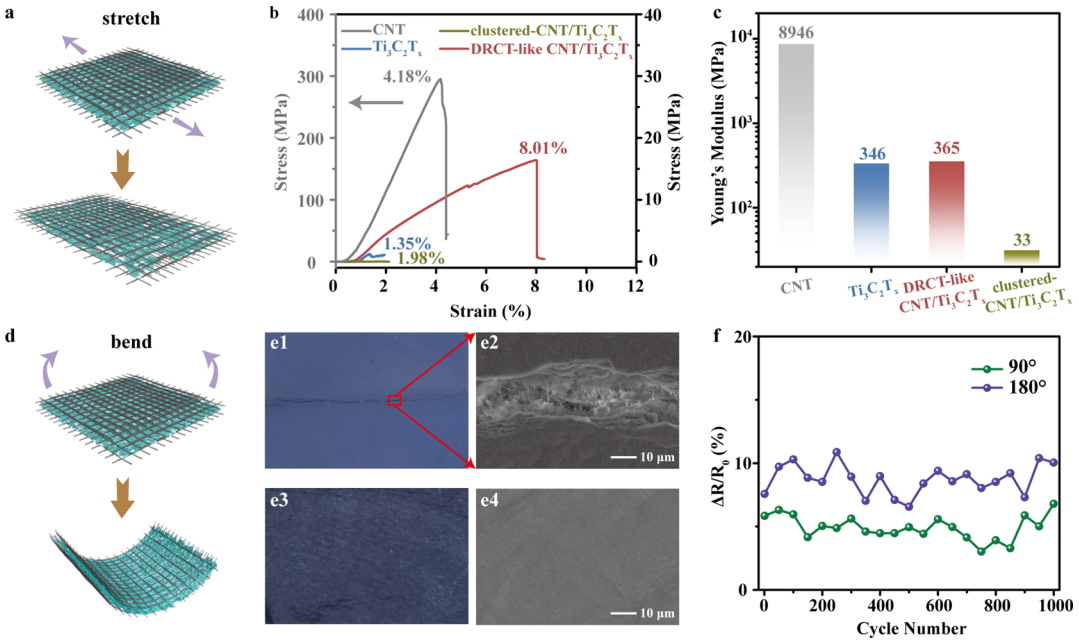

Figure 3. Stretching and bending mechanical properties of films. (a) Schematic of tensile test for the DRCT-like CNT/Ti_3C_2 film. (b) Stress–strain curves. (c) Young's modulus. (d) Schematic of bending test for the DRCT-like CNT/Ti_3C_2 film. (e1) Optical microscopy and (e2) SEM images of Ti_3C_2 film after bending. (e3) Optical microscopy and (e4) SEM images of the DRCT-like CNT/Ti_3C_2 film after bending. (f) Normalized resistance changes of the DRCT-like CNT/Ti_3C_2 film during 1000 cycles at 90° and 180° bending.

followed by 30 min of relaxation. The lithium-ion diffusion coefficient D_{Li+} was calculated based on the delithiation process to avoid the influence of SEI.[42] Battery performance was tested using the Land battery system (Wuhan Land Electronic Co., China) with a voltage range of 0.01−3 V. The testing environment at −40 °C was maintained by a temperature chamber (Nanjing Modges Energy Technology Co., China). For the CNT anode, the specific capacity of the battery was calculated based on the mass of CNT. For other anodes, the specific capacity was calculated based on the mass of Ti_3C_2.

2.10. Calculation. DFT calculations were conducted using the DMol3 package in Materials Studio, applying the Generalized Gradient Approximation (GGA) of Perdew–Burke–Ernzerhof (PBE) for the exchange–correlation energy. All models underwent full optimization before the calculation of the electronic properties. The Ti_3C_2 monolayer was simulated by a (3 × 3 × 1) supercell for (001) surface with a vacuum thickness of 15 Å. A carbon layer with a side length of 9.52 Å was added to establish the model of the CNT/Ti_3C_2 composite, where the spacing between the carbon layer and Ti_3C_2 was optimized. In both models, a single Li atom was introduced at multiple sites, and the adsorption energy (E_a) was calculated as follows:

$$E_a = E_{sub+Li} - (E_{sub} + E_{Li})$$

where E_{sub+Li} represents the total energy of the substrate with a single Li adsorbed, E_{sub} denotes the energy of the substrate, and E_{Li} is the energy of a single Li atom in the unit cell of lithium crystal.[43]

3. RESULTS AND DISCUSSION

Ti_3C_2 possessed an accordion-like layered structure (Figure S1a), and the TEM images revealed a spindle shape with a lattice spacing of 0.49 nm (Figure S1b,c), corresponding to the (004) plane.[44−48] The employment of direct vacuum filtration on the Ti_3C_2 aqueous dispersion resulted in a densely stacked membrane (Figure S2a,d). It was a mechanically fragile structure comprised of numerous small clusters. From an electrochemical perspective, such dense stacking significantly diminished the accessible surface area of Ti_3C_2, thereby obstructing the thorough penetration of lithium ions into its interlayers and consequently reducing its lithium storage capability. Furthermore, the attempt to directly amalgamate SACNTs with Ti_3C_2 utilizing ultrasonication followed by vacuum filtration did not culminate in a homogeneous composite, as depicted in Figures S2b and S2e. Instead, Ti_3C_2 and CNTs predominantly congregated into distinct agglomerates, and this product was named a clustered-CNT/Ti_3C_2 film.

Herein, a biomimetic DRCT-like CNT/Ti_3C_2 composite was constructed through an alternating assembly approach (Figure 2a). The process was initiated with the ultrasonic dispersion of Ti_3C_2 in an aqueous medium, which was divided into 10 equal portions. Subsequently, macrosized SACNT films were extracted from the array and arranged in a perpendicular cross-layering manner at 90°. This was followed by the execution of 10 cycles of alternating vacuum filtration involving the Ti_3C_2 aqueous dispersion and striped SACNT membranes, culminating in the creation of a specimen designated as DRCT-like CNT/Ti_3C_2-10. The striped SACNT membrane uniformly covered the surface (Figure S2c) and facilitated the expansion of the interlayer spacing within Ti_3C_2 (Figures 2b and S2e). In this architecture, SACNTs are similar to "fibers" to provide mechanical support and transport channels, while Ti_3C_2 materials are uniformly dispersed in this framework for energy storage. By modulation of the portions of Ti_3C_2 dispersion and the frequency of vacuum filtration, it is possible to precisely engineer the compositional organization of Ti_3C_2 and CNTs, which influences the mechanical and electrochemical properties of the composites. For the purpose of comparative analysis, additional variants, namely, DRCT-like CNT/Ti_3C_2-2 and DRCT-like CNT/Ti_3C_2-20 were also prepared.

To further investigate the composition and structure of the films, comprehensive analyses were conducted using XRD, Raman spectroscopy, and TEM. According to the XRD results,

https://doi.org/10.1021/acsaem.4c01650
ACS Appl. Energy Mater. 2024, 7, 8004−8013

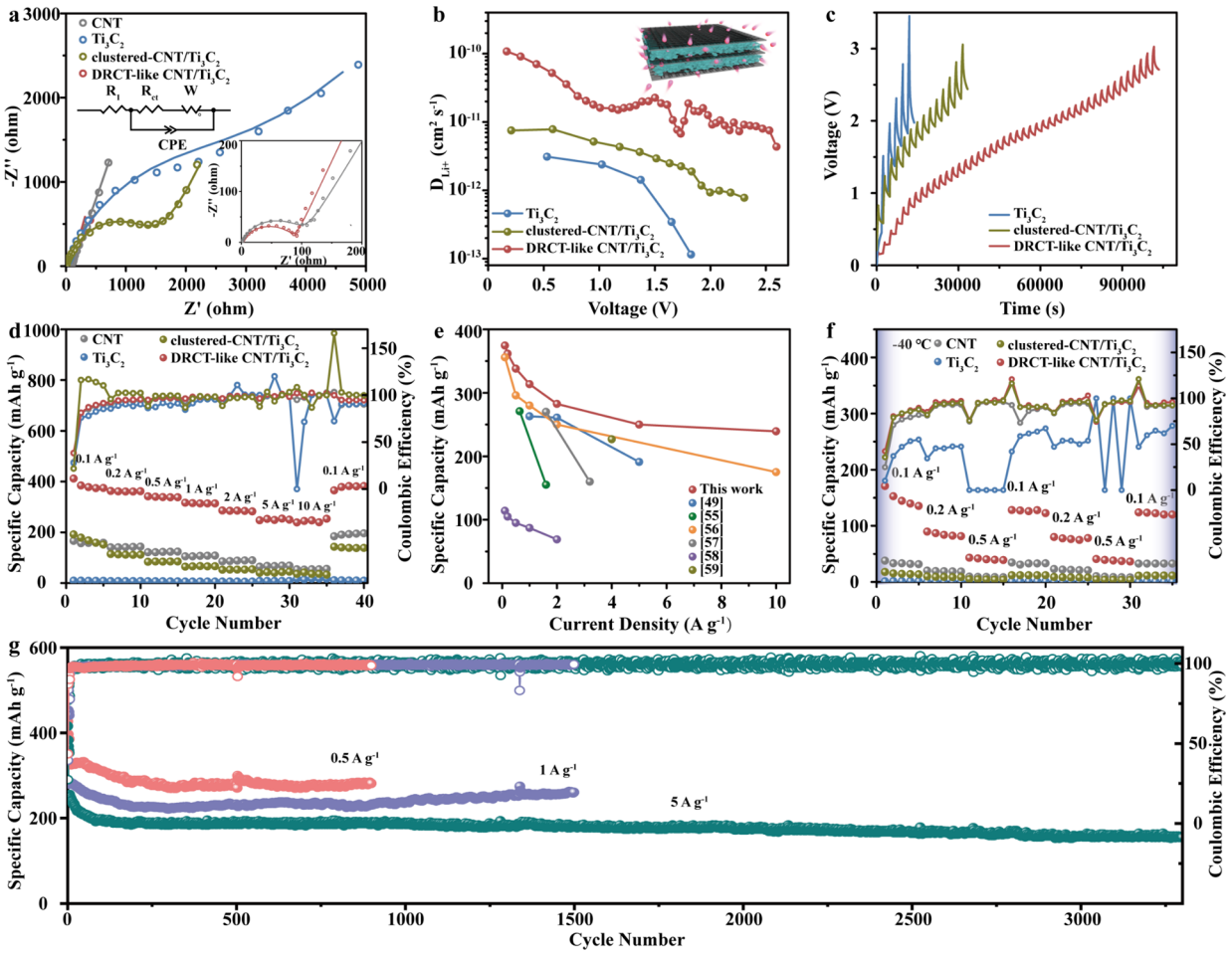

Figure 4. Electrochemical performance of films at 25 and −40 °C. (a) EIS profiles of CNT, Ti_3C_2, clustered-CNT/Ti_3C_2, and DRCT-like CNT/Ti_3C_2 anodes. (b) D_{Li+} of Ti_3C_2, clustered-CNT/Ti_3C_2 and DRCT-like CNT/Ti_3C_2 anodes. (c) GITT profiles of Ti_3C_2, clustered-CNT/Ti_3C_2, and DRCT-like CNT/Ti_3C_2 anodes during the first charging process. (d) Rate performance of CNT, Ti_3C_2, clustered-CNT/Ti_3C_2, and DRCT-like CNT/Ti_3C_2 anodes. (e) Specific capacity and current density comparison with other literature. (f) Rate performance of CNT, Ti_3C_2, clustered-CNT/Ti_3C_2, and DRCT-like CNT/Ti_3C_2 anodes at −40 °C. (g) Cycle performance of the DRCT-like CNT/Ti_3C_2 anode.

the striped SACNT membrane displayed a prominent peak at approximately 25° (Figure S3), while the Ti_3C_2 film manifested a peak around 6.7°, indicative of its (002) crystal plane.[49] These peaks were also observed in the clustered-CNT/Ti_3C_2 and DRCT-like CNT/Ti_3C_2 films. In the Raman spectroscopy (Figure 2c), the CNT film showcased three peaks: 1354.0 cm^{-1} (D band) linked to defects, 1584.2 cm^{-1} (G band) corresponding to signals from graphite, and 2699.8 cm^{-1} (2D band) associated with double resonant Raman scattering and two-phonon emissions.[50] The Ti_3C_2 film possessed five characteristic peaks, including 200, 400, and 600 cm^{-1} peaks, which are indicative of vibrations from Ti_3C_2, as well as D and G bands.[51,52] Both clustered-CNT/Ti_3C_2 and DRCT-like CNT/Ti_3C_2 films featured typical peaks of CNTs and Ti_3C_2. Second, vacuum filtration was executed on a 4-layered striped SACNT membrane and the Ti_3C_2 dispersion for TEM characterization. The TEM image vividly showcased a DRCT structure (Figure 2d). Cross-arranged CNTs established a robust mechanical framework and a conductive network. Meanwhile, spindle-shaped Ti_3C_2, with diameters ranging from 30 to 70 nm, was dispersed uniformly throughout the interwoven CNTs. EDS mapping of the SEM and TEM images of the DRCT-like CNT/Ti_3C_2 film revealed a uniform distribution of Ti and C elements (Figure S4). The analyses of XRD, Raman, and TEM characterization consistently confirm that in the DRCT-like CNT/Ti_3C_2 film, CNTs, and Ti_3C_2 are seamlessly integrated and uniformly distributed.

These films underwent tensile testing at a strain rate of 1% min^{-1} to evaluate their stretch resistance capabilities (Figure 3a−c). The strain values for CNT, Ti_3C_2, clustered-CNT/Ti_3C_2, and DRCT-like CNT/Ti_3C_2 films were measured at 4.18, 1.35, 1.98, and 8.01%, respectively, with corresponding Young's modulus values of 8,946, 346, 33, and 365 MPa. Among them, the Ti_3C_2 film exhibited the earliest onset of failure. Mechanically, the tensile stress applied to the Ti_3C_2 film relies on shear stress transmission between overlapping flakes as well as the self-deformation. The former readily engenders critical transverse cracks at junctions of adjacent flakes, leading to rapid structural failure.[53] As for the clustered-CNT/Ti_3C_2 film, it also demonstrated limited tensile strain endurance, mainly because a considerable portion of Ti_3C_2 remained in a stacked configuration (Figure S2b,e). This resulted in a failure mechanism similar to that of the Ti_3C_2 film. In contrast, the DRCT-like CNT/Ti_3C_2 film exhibited impressive resilience, withstanding strains of up to 8.01%. This remarkable performance can be attributed to the striped SACNT membranes. They effectively serve as an elastic mechanical framework, capable of handling tensile stress and

https://doi.org/10.1021/acsaem.4c01650
ACS Appl. Energy Mater. 2024, 7, 8004−8013

preventing premature structural failure. The incorporation of striped SACNT membranes notably improved the strain tolerance of the material, increasing it from 1.35 to 8.01%, underscoring the effectiveness of the DRCT-like structure in enhancing mechanical tensile strength. In addition, tensile tests were also performed on DRCT-like CNT/Ti_3C_2 films with different layer numbers (Figure S5). The strains of DRCT-like CNT/Ti_3C_2-2 and CNT/Ti_3C_2-20 films were 1.72 and 10.57%, and the Young's moduli were 263 and 532 MPa, respectively. It indicates that a higher proportion of CNTs within this structure can further improve its tensile performance.

Subsequent investigations focused on the bending properties of the films (Figure 3d–f). Initially, both the Ti_3C_2 and DRCT-like CNT/Ti_3C_2 films were subjected to a single 180° bend. According to the results of optical microscopy and SEM (Figure 3e1,2), obvious cracks appeared on the surface of the Ti_3C_2 film accompanied by interlayer detachment. In contrast, the surface structure of the DRCT-like CNT/Ti_3C_2 film remained unchanged (Figure 3e3,4). Subsequently, multiple bendings at 90° and 180° were applied to the DRCT-like CNT/Ti_3C_2 film, with real-time measurement of the resistance change (Figure 3f). Impressively, the resistance remained stable throughout the long bending process. Even after 1000 bending cycles at 90° and 180°, the DRCT-like CNT/Ti_3C_2 film displayed minimal resistance increments of 6.8 and 10.0%, respectively, and maintained its structural integrity (Figure S6). Therefore, in the DRCT-like CNT/Ti_3C_2 film, highly flexible striped SACNT membranes effectively endure large-angle and long-term bending, thereby preserving the integrity of the Ti_3C_2 layers.

In the DRCT-like CNT/Ti_3C_2 film, the CNT "fibers" not only serve as a robust mechanical scaffold but also facilitate the exposure of abundant active sites of Ti_3C_2, which is expected to improve the reaction kinetics and electrochemical performance when used as the anode. EIS measurements were conducted on a series of anodes to investigate the kinetics at the anode/electrolyte interface (Figures 4a, S7, and Table S1). The Ti_3C_2 and clustered-CNT/Ti_3C_2 anodes had significant charge transfer resistance (R_{ct}) of 3256.0 and 1572.0 Ω, respectively. This may be due to the significant stacking of Ti_3C_2, which hinders the transfer of lithium ions at the anode/electrolyte interface. The R_{ct} for the DRCT-like CNT/Ti_3C_2-2 anode was also relatively high (676.8 Ω), which could be attributed to inadequate layer separation from minimal filtration cycles. For the DRCT-like CNT/Ti_3C_2-10 and DRCT-like CNT/Ti_3C_2-20 anodes, the R_{ct} was significantly reduced to 84.3 and 78.4 Ω, respectively. It indicated that the R_{ct} of the anode gradually decreased as the CNT ratio and the number of laminations increased.

Subsequently, galvanostatic intermittent titration technique (GITT) experiments were carried out to explore the internal dynamics of the anodes (Figure 4b,c). Pulsed currents were applied to the Ti_3C_2, clustered-CNT/Ti_3C_2, and DRCT-like CNT/Ti_3C_2 anodes, discharging from open circuit voltage to 0.01 V, followed by charging up to 3 V. The pulse current was set at 0.1 A g^{-1} with each lasting 10 min, and a 30 min interval between pulses was allowed to enable electrode relaxation. To mitigate the influence of the solid electrolyte interphase (SEI), the calculation of the lithium-ion diffusion coefficient D_{Li+} was based on the first charging process. Detailed voltage curves and specific calculation methods are illustrated in Figure S8. The measurements indicate a gradual decrease in D_{Li+} during the charging process, in agreement with other established findings.[54] Among these anodes, Ti_3C_2 exhibited the lowest D_{Li+}, probably because the densely packed layers hindered the efficient insertion and diffusion of lithium ions. For the clustered-CNT/Ti_3C_2 anode, there was a slight increase in D_{Li+}, estimated to be around 10^{-11}–10^{-12} cm^2 s^{-1}. Moreover, the D_{Li+} of the DRCT-like CNT/Ti_3C_2 anode was further increased to the range 10^{-10}–10^{-11} cm^2 s^{-1}. These findings confirm that the DRCT-like structure can significantly accelerate lithium ion diffusion within the electrode, indicating its potential for excellent electrochemical performance.

At ambient temperature, a rate test was conducted on four types of anodes (Figure 4d), with current densities ranging from 0.1 to 10 A g^{-1}. The Ti_3C_2 anode struggled with lithium-ion deintercalation, exhibiting a negligible specific capacity. At a current density of 0.1 A g^{-1}, the specific capacities of the CNT and clustered-CNT/Ti_3C_2 anodes were 158.8 and 151.7 mA h g^{-1}, respectively. However, their capacities significantly decreased at 10 A g^{-1}, with a capacity retention of only 34.9% (55.5 mA h g^{-1}/158.8 mA h g^{-1}) and 22.0% (33.3 mA h g^{-1}/151.7 mA h g^{-1}), correspondingly. Conversely, the DRCT-like CNT/Ti_3C_2 anode exhibited an exceptional rate performance. At current densities of 0.1, 0.2, 0.5, 1, 2, 5, and 10 A g^{-1}, the specific capacities of the DRCT-like CNT/Ti_3C_2 anode were 374.5, 361.8, 338.1, 313.6, 282.5, 253.6, and 253.1 mA h g^{-1}, respectively. This proves that the DRCT-like structure enlarges lithium storage sites, thereby elevating the capacity. Additionally, rate tests were carried out on DRCT-like CNT/Ti_3C_2-2 and DRCT-like CNT/Ti_3C_2-20 anodes (Figure S9). The DRCT-like CNT/Ti_3C_2-2 anode showcased a specific capacity of 254.0 mA h g^{-1} at 0.1 A g^{-1}, which was reduced to 78.0 mA h g^{-1} at 10 A g^{-1}. This reduction can be attributed to continuous stacking within the electrode, leading to a diminished insertion site for lithium ions. The DRCT-like CNT/Ti_3C_2-20 anode performed best at low current densities. However, as the current density increased, its performance deteriorated rapidly. Specifically, at 5 and 10 A g^{-1}, the specific capacities of the anode were 255.0 and 201.8 mA h g^{-1}, respectively. This phenomenon may be attributed to excessive layers within the electrode. At low current densities, efficient charge transfer and ion diffusion within the electrode can produce a high capacity. Conversely, at high current densities, excessive delamination may hinder rapid ion diffusion between layers, resulting in a reduced capacity. In summary, the three-dimensional DRCT-like structure can extend lithium storage sites in Ti_3C_2 and improve lithium storage capacity, while the number of layers (or electrode thickness) needs to be optimized. The DRCT-like CNT/Ti_3C_2-10 anode demonstrated the best rate performance and also compared favorably with other MXene anodes (Figure 4e and Table S2),[49,50,52,55–57] thereby being selected for subsequent experiments.

In addition to behaviors at various current densities, the long-term cycling stability of the battery is also crucial. Here, the DRCT-like CNT/Ti_3C_2 anode was initially activated at a modest current density of 0.1 A g^{-1} for 5 cycles, followed by cycling at 0.5, 1, and 5 A g^{-1} (Figure 4g). Upon raising the current density from 0.1 to 0.5 A g^{-1}, the specific capacity of the DRCT-like CNT/Ti_3C_2 anode was 327.7 mA h g^{-1}, and it sustained 281.5 mA h g^{-1} after 895 cycles. At an increased current density of 1 A g^{-1}, the DRCT-like CNT/Ti_3C_2 anode exhibited specific capacities of 279.4 mA h g^{-1} at the 6th cycle and 261.1 mA h g^{-1} at the 1500th cycle. Further increasing the

https://doi.org/10.1021/acsaem.4c01650
ACS Appl. Energy Mater. 2024, 7, 8004–8013

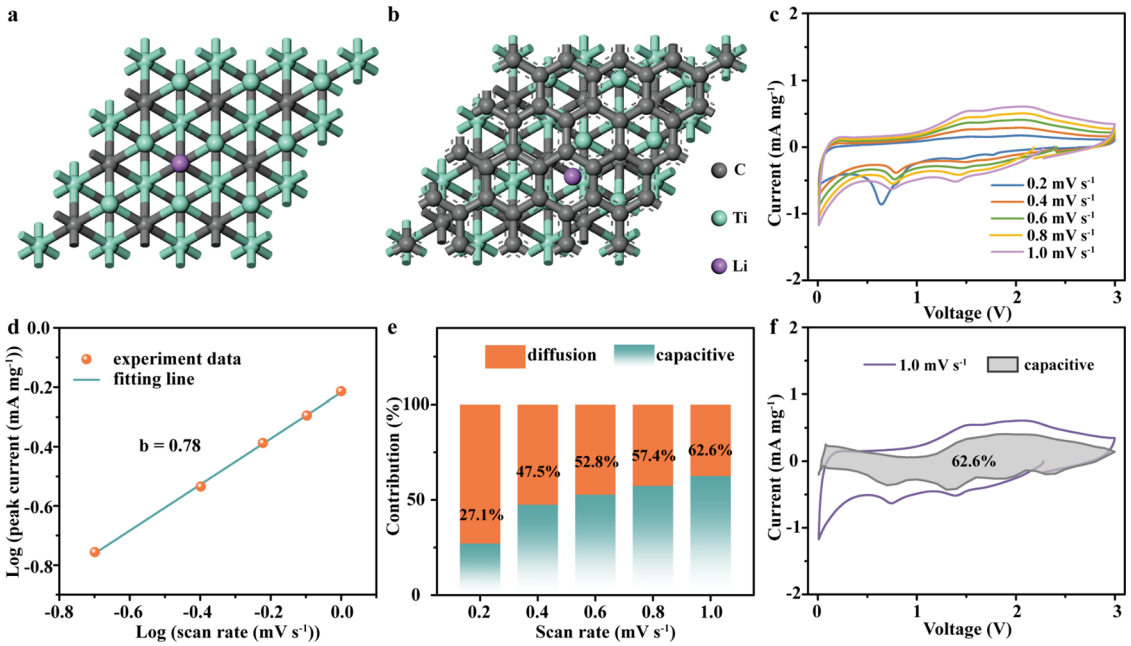

Figure 5. Computational and experimental investigation of the lithium storage mechanism. (a) Top views of the optimized Li-adsorbed Ti_3C_2 and (b) CNT/Ti_3C_2 models. (c) CV profiles of a DRCT-like CNT/Ti_3C_2 anode at various scan rates. (d) *b*-value determination of the peaks in CV profiles. (e) Percentage of capacitive contribution of a DRCT-like CNT/Ti_3C_2 anode. (f) Capacitive current contribution to charge storage (scan rate: 1 mV s^{-1}).

current density to 5 A g^{-1}, the anode achieved a specific capacity of 255.5 mA h g^{-1} at the 6th cycle and maintained 154.5 mA h g^{-1} even after 3295 cycles, indicating a minimal capacity decay of approximately 0.01% per cycle. This exceptional performance underscores the robust structural and electrochemical stability of the DRCT-like CNT/Ti_3C_2 anode.

The merits of this structural design were distinctly evident even under the challenging conditions of a low temperature. Generally, low temperatures lead to sluggish kinetics and decreased capacity of electrodes.[58] The electrochemical performance of the four anodes was evaluated at −40 °C (Figures 4f and S10). Both Ti_3C_2 and clustered-CNT/Ti_3C_2 anodes faced considerable challenges in the insertion and extraction of lithium ions, leading to negligible capacities. For the CNT anode, its specific capacity was merely 31.6 mA h g^{-1} at 0.1 A g^{-1} and further decreased as the current density increased. In contrast, the DRCT-like CNT/Ti_3C_2 anode exhibited specific capacities of 135.5, 81.4, and 38.9 mA h g^{-1} at current densities of 0.1, 0.2, and 0.5 A g^{-1}, respectively. Impressively, after serial cycles at these current densities, the DRCT-like CNT/Ti_3C_2 anode showcased high specific capacity retention, reaching 90.3% (122.4 mA h g^{-1}/ 135.5 mA h g^{-1}), 95.8% (78.0 mA h g^{-1}/ 81.4 mA h g^{-1}), and 93.6% (36.4 mA h g^{-1}/38.9 mA h g^{-1}) at 0.1, 0.2, and 0.5 A g^{-1}, correspondingly. This outstanding electrochemical performance underscores the efficacy of the DRCT-like structure in boosting ion-electron transport, thereby improving electrode kinetics under cold conditions.

According to the above results, the DRCT-like CNT/Ti_3C_2 anode exhibits a superior electrochemical performance at both ambient and low temperatures. To gain insights into the origins of the remarkable performance, DFT calculations, and CV tests were employed to analyze the lithium storage mechanism.

Models of Ti_3C_2 and CNT/Ti_3C_2 were constructed to assess their lithium adsorption energies. The interlayer spacing between carbon and Ti_3C_2 layers in the CNT/Ti_3C_2 model was optimized (Figure S11), and the most favorable adsorption site of Li on both models was discussed (Figure S12). In the Ti_3C_2 model, lithium adsorption was assessed at three high-symmetry sites (Figure S12a): above the carbon atom (site 1), above the top titanium atom (site 2), and above the middle titanium atom (site 3). Calculations revealed that for the Ti_3C_2 model, site 1 was the preferred lithium adsorption site due to its minimal adsorption energy (Figure S13a−c). In the optimized model (Figure 5a), the Li−C distance was 3.550 Å and the adsorption energy was −0.394 eV, aligning closely with prior computational results.[5] For the CNT/Ti_3C_2 model, the adsorption of Li to these three sites was also investigated (Figure S12b), with site 3 emerging as the most advantageous site (Figure S13d−f). Compared with the adsorption energy of Ti_3C_2 for Li (−0.394 eV), CNT/Ti_3C_2 had lower adsorption energy (−0.914 eV, Figure 5b), indicating that the incorporation of carbon layers enhanced the natural affinity with lithium atoms and promoted electrochemical storage efficiency.

Afterward, the CV test was conducted on the DRCT-like CNT/Ti_3C_2 anode at varying scan rates, with the voltage range of 0.01−3.0 V vs Li/Li^+ (Figure 5c). At a scan rate of 0.2 mV s^{-1}, the anode displayed a reduction peak around 0.6 V, which disappeared in subsequent cycles. This reduction peak corresponds to the electrolyte decomposition and the formation of SEI. Furthermore, the broad oxidation and reduction peaks near 1.5 and 2.0 V could be attributed to the reversible lithiation and delithiation processes of Ti_3C_2.[49,52] Notably, the peak currents in the CV curves exhibit the following relationship with the scan rate.[49]

$$i = av^b (0.5 \leq b \leq 1) \quad (1)$$

https://doi.org/10.1021/acsaem.4c01650
ACS Appl. Energy Mater. 2024, 7, 8004−8013

$$\log(i) = b \times \log(v) + \log(a) \quad (2)$$

where "i" represents peak current, "v" signifies scan rate, and coefficients "a" and "b" can be determined through a linear fit of $\log(i)$ and $\log(v)$ using formula 2. The parameter "b" is crucial in characterizing the lithium storage mechanism within the electrode: b = 0.5 corresponds to a pure diffusion contribution, b = 1 indicates a completely capacitive contribution, and a value between 0.5 and 1 implies a combination of both diffusion and capacitive mechanism. Upon fitting the $\log(i)$−$\log(v)$ curve of the oxidation peak near 2.0 V, a robust linear relationship was observed, yielding a value of "b" equal to 0.78 (Figure 5d). Consequently, it can be concluded that in the lithium storage process of the DRCT-CNT/Ti_3C_2 anode, there is a coexistence of both diffusion and capacitive contributions.

Furthermore, the proportion of energy storage in these two forms can be quantified using Dunn's method.[59] During CV scanning, the total current "i" can be deconstructed into two separate components: a diffusion-controlled portion ($k_2v^{1/2}$) and a capacitance-controlled portion (k_1v). This relationship can be mathematically represented as follows:

$$i = k_1v + k_2v^{1/2} \quad (3)$$

$$\frac{i}{v^{1/2}} = k_1v^{1/2} + k_2 \quad (4)$$

Through linear fitting of $i/v^{1/2}$ and $v^{1/2}$ at different scan rates, the ratio of diffusive and capacitive contributions can be determined. Based on this method, it has been calculated that as the scan rate increased from 0.2 to 1.0 mV s^{-1}, the capacitive contribution of the anode gradually rose from 27.1 to 62.6% (Figure 5e). Additionally, Figure 5f presents the original CV curve at 1.0 mV s^{-1} (purple line) along with the capacitive contribution obtained from the fitting (shaded area). These findings highlight the predominant role of the capacitive contribution in the DRCT-like CNT/Ti_3C_2 anode. On the one hand, this is attributed to the lithium storage mechanism of Ti_3C_2, which involves the reversible intercalation/deintercalation of lithium ions and theoretically offers a high pseudocapacitance contribution. On the other hand, the multilayer insertion of the striped SACNT membrane helps to partially separate the Ti_3C_2 layers, thereby exposing more accessible active sites and enhancing electrode kinetics.

4. CONCLUSIONS

MXene materials are highly regarded for their potential in LIBs, whereas their practical applications have been constrained by layer stacking. In this research, a biomimetic composite was devised with a DRCT-like structure using SACNTs and the representative MXene material Ti_3C_2. The SACNTs "fibers" provide mechanical support and enhance ion-electron transport dynamics, while the Ti_3C_2 "cells" are uniformly dispersed, with stacking suppressed and energy storage efficacy enhanced. This room-temperature synthesis method is straightforward and adjustable, resulting in a DRCT-like CNT/Ti_3C_2 composite with superior mechanical and electrochemical properties. In terms of mechanics, the DRCT-like CNT/Ti_3C_2 film could withstand strains of up to 8.01%. During 1000 bending cycles at 90° and 180°, the resistance increment of the film was stabilized at approximately 7 and 10%, respectively. Regarding electrochemistry, EIS and GITT tests revealed swift lithium-ion transfer and diffusion both at the interface and within the anode. At room temperature, the anode attained a specific capacity of 253.1 mA h g^{-1} at a high current density of 10 A g^{-1} and showcased stable cycling for 3300 cycles. Moreover, the lithium storage performance of the Ti_3C_2 system was tested at −40 °C for the first time. In addition, the lithium storage mechanism was elucidated through DFT calculations and CV measurement. DFT calculations revealed the role of the carbon layer in reducing the adsorption energy of Ti_3C_2, thereby enhancing its natural affinity with Li. The CV test confirmed the existence of diffusive and capacitive energy storage mechanisms, with the capacitive contribution increasing to 62.6% at a scan rate of 1 mV s^{-1}. This biomimetic DRCT-like structure presents an innovative solution to the stacking dilemma, unlocking the full potential of two-dimensional materials for advanced energy storage applications.

■ ASSOCIATED CONTENT

Supporting Information

The Supporting Information is available free of charge at https://pubs.acs.org/doi/10.1021/acsaem.4c01650.

SEM images, XRD pattern, mechanical tensile properties, EIS profiles, illustration of the GITT calculation, rate performance, electrochemical performance at −40 °C, model optimization, and performance comparison (PDF)

■ AUTHOR INFORMATION

Corresponding Authors

Jiaping Wang − *Department of Physics and Tsinghua-Foxconn Nanotechnology Research Center, Tsinghua University, Beijing 100084, China; Frontier Science Center for Quantum Information, Beijing 100084, China;* orcid.org/0000-0002-8300-4992; Email: jpwang@tsinghua.edu.cn

Peng Liu − *Department of Physics and Tsinghua-Foxconn Nanotechnology Research Center, Tsinghua University, Beijing 100084, China;* orcid.org/0000-0002-1860-5126; Email: pengliu@mail.tsinghua.edu.cn

Authors

Zixin Hong − *Department of Physics and Tsinghua-Foxconn Nanotechnology Research Center, Tsinghua University, Beijing 100084, China*

Hui Tian − *Department of Physics and Tsinghua-Foxconn Nanotechnology Research Center, Tsinghua University, Beijing 100084, China*

Zhenhan Fang − *Department of Physics and Tsinghua-Foxconn Nanotechnology Research Center, Tsinghua University, Beijing 100084, China*

Hengcai Wu − *Department of Physics and Tsinghua-Foxconn Nanotechnology Research Center, Tsinghua University, Beijing 100084, China*

Fei Zhao − *Department of Physics and Tsinghua-Foxconn Nanotechnology Research Center, Tsinghua University, Beijing 100084, China*

Qunqing Li − *Department of Physics and Tsinghua-Foxconn Nanotechnology Research Center, Tsinghua University, Beijing 100084, China; Frontier Science Center for Quantum Information, Beijing 100084, China;* orcid.org/0000-0001-9565-0855

https://doi.org/10.1021/acsaem.4c01650
ACS Appl. Energy Mater. 2024, 7, 8004−8013

Shoushan Fan − *Department of Physics and Tsinghua-Foxconn Nanotechnology Research Center, Tsinghua University, Beijing 100084, China*

Complete contact information is available at: https://pubs.acs.org/10.1021/acsaem.4c01650

Author Contributions

The manuscript was written through the contributions of all authors. All authors have given approval to the final version of the manuscript.

Notes

The authors declare no competing financial interest.

■ ACKNOWLEDGMENTS

This work was supported by the National Basic Research Program of China (2019YFA0705702) and the National Natural Science Foundation of China (51872158).

■ REFERENCES

(1) Naguib, M.; Kurtoglu, M.; Presser, V.; Lu, J.; Niu, J.; Heon, M.; Hultman, L.; Gogotsi, Y.; Barsoum, M. W. Two-Dimensional Nanocrystals Produced by Exfoliation of Ti_3AlC_2. *Adv. Mater.* **2011**, *23* (37), 4248−4253.

(2) Zhang, Y.; Yan, Y.; Qiu, H.; Ma, Z.; Ruan, K.; Gu, J. A Mini-Review of MXene Porous Films: Preparation, Mechanism and Application. *J. Mater. Sci. Technol.* **2022**, *103*, 42−49.

(3) Fan, Z.; Wang, Y.; Xie, Z.; Wang, D.; Yuan, Y.; Kang, H.; Su, B.; Cheng, Z.; Liu, Y. Modified MXene/Holey Graphene Films for Advanced Supercapacitor Electrodes with Superior Energy Storage. *Adv. Sci.* **2018**, *5* (10), No. 1800750.

(4) Sun, D.; Wang, M.; Li, Z.; Fan, G.; Fan, L.-Z.; Zhou, A. Two-Dimensional Ti_3C_2 as Anode Material for Li-Ion Batteries. *Electrochem. commun.* **2014**, *47*, 80−83.

(5) Tang, Q.; Zhou, Z.; Shen, P. Are MXenes Promising Anode Materials for Li Ion Batteries? Computational Studies on Electronic Properties and Li Storage Capability of Ti_3C_2 and $Ti_3C_2X_2$ (X = F, OH) Monolayer. *J. Am. Chem. Soc.* **2012**, *134* (40), 16909−16916.

(6) Mathis, T. S.; Maleski, K.; Goad, A.; Sarycheva, A.; Anayee, M.; Foucher, A. C.; Hantanasirisakul, K.; Shuck, C. E.; Stach, E. A.; Gogotsi, Y. Modified MAX Phase Synthesis for Environmentally Stable and Highly Conductive Ti_3C_2 MXene. *ACS Nano* **2021**, *15* (4), 6420−6429.

(7) Xiong, D.; Li, X.; Bai, Z.; Lu, S. Recent Advances in Layered $Ti_3C_2T_x$ MXene for Electrochemical Energy Storage. *Small* **2018**, *14* (17), No. 1703419.

(8) Li, Y.; Wang, R.; Guo, Z.; Xiao, Z.; Wang, H.; Luo, X.; Zhang, H. Emerging Two-Dimensional Noncarbon Nanomaterials for Flexible Lithium-Ion Batteries: Opportunities and Challenges. *J. Mater. Chem. A* **2019**, *7* (44), 25227−25246.

(9) Toyoura, K.; Koyama, Y.; Kuwabara, A.; Tanaka, I. Effects of Off-Stoichiometry of LiC_6 on the Lithium Diffusion Mechanism and Diffusivity by First Principles Calculations. *J. Phys. Chem. C* **2010**, *114* (5), 2375−2379.

(10) Dimitrov, I. K.; Manley, M. E.; Shapiro, S. M.; Yang, J.; Zhang, W.; Chen, L. D.; Jie, Q.; Ehlers, G.; Podlesnyak, A.; Camacho, J.; Li, Q. Einstein Modes in the Phonon Density of States of the Single-Filled Skutterudite $Yb_{0.2}Co_4Sb_{12}$. *Phys. Rev. B: Condens. Matter Mater. Phys.* **2010**, *82* (17), No. 174301.

(11) Marinho, B.; Ghislandi, M.; Tkalya, E.; Koning, C. E.; de With, G. Electrical Conductivity of Compacts of Graphene, Multi-Wall Carbon Nanotubes, Carbon Black, and Graphite Powder. *Powder Technol.* **2012**, *221*, 351−358.

(12) Yi, T.-F.; Wei, T.-T.; Li, Y.; He, Y.-B.; Wang, Z.-B. Efforts on Enhancing the Li-Ion Diffusion Coefficient and Electronic Conductivity of Titanate-Based Anode Materials for Advanced Li-Ion Batteries. *Energy Storage Mater.* **2020**, *26*, 165−197.

(13) Li, K.; Wang, X.; Li, S.; Urbankowski, P.; Li, J.; Xu, Y.; Gogotsi, Y. An Ultrafast Conducting Polymer@MXene Positive Electrode with High Volumetric Capacitance for Advanced Asymmetric Supercapacitors. *Small* **2020**, *16* (4), No. 1906851.

(14) Lukatskaya, M. R.; Kota, S.; Lin, Z.; Zhao, M.-Q.; Shpigel, N.; Levi, M. D.; Halim, J.; Taberna, P.-L.; Barsoum, M. W.; Simon, P.; Gogotsi, Y. Ultra-High-Rate Pseudocapacitive Energy Storage in Two-Dimensional Transition Metal Carbides. *Nat. Energy* **2017**, *2* (8), 17105.

(15) Deng, Y.; Shang, T.; Wu, Z.; Tao, Y.; Luo, C.; Liang, J.; Han, D.; Lyu, R.; Qi, C.; Lv, W.; Kang, F.; Yang, Q.-H. Fast Gelation of $Ti_3C_2T_x$ MXene Initiated by Metal Ions. *Adv. Mater.* **2019**, *31* (43), No. 1902432.

(16) Zhang, Y.; Wang, B.; Gao, S.; Qiu, L.; Zheng, Q.; Cheng, G.; Han, W.; Ramakrishna, S.; Long, Y. Electrospun MXene Nanosheet/Polymer Composites for Electromagnetic Shielding and Microwave Absorption: A Review. *ACS Appl. Nano Mater.* **2022**, *5* (9), 12320−12342.

(17) Zhou, G.; Li, M.; Liu, C.; Wu, Q.; Mei, C. 3D Printed $Ti_3C_2T_x$ MXene/Cellulose Nanofiber Architectures for Solid-state Supercapacitors: Ink Rheology, 3D Printability, and Electrochemical Performance. *Adv. Funct. Mater.* **2022**, *32* (14), No. 2109593.

(18) Kou, W.; Yu, L.; Wang, Q.; Yang, Y.; Yang, T.; Geng, H.; Miao, X.; Gao, B.; Yang, G. Enhanced Zn^{2+} Transfer Dynamics via a 3D Bird Nest-like VO_2/MXene Heterojunction for Ultrahigh-Rate Aqueous Zinc-Ion Batteries. *J. Power Sources* **2022**, *520*, No. 230872.

(19) Zhao, M.; Ren, C. E.; Ling, Z.; Lukatskaya, M. R.; Zhang, C.; Van Aken, K. L.; Barsoum, M. W.; Gogotsi, Y. Flexible MXene/Carbon Nanotube Composite Paper with High Volumetric Capacitance. *Adv. Mater.* **2015**, *27* (2), 339−345.

(20) Mohajer, F.; Ziarani, G. M.; Badiei, A.; Iravani, S.; Varma, R. S. MXene-Carbon Nanotube Composites: Properties and Applications. *Nanomaterials* **2023**, *13* (2), 345.

(21) Dang, A.; Sun, Y.; Liu, Y.; Xia, Y.; Liu, X.; Gao, Y.; Wu, S.; Li, T.; Zada, A.; Ye, F. Flexible $Ti_3C_2T_x$/Carbon Nanotubes/CuS Film Electrodes Based on a Dual-Structural Design for High-Performance All-Solid-State Supercapacitors. *ACS Appl. Energy Mater.* **2022**, *5* (7), 9158−9172.

(22) Dang, A.; Han, Y.; Sun, Y.; Liu, Y.; Zhao, Z.; Liu, X.; Zada, A.; Han, Y.; Li, T.; Li, J. Mechanically Stable Reduced Graphene Oxide/MXene Fibers with Exceptional Volumetric Capacitance and Energy Density Mediated by Carbon Nanotubes for High-Performance Symmetrical Supercapacitors. *ACS Appl. Energy Mater.* **2024**, *7* (13), 5548−5558.

(23) Dang, A.; Sun, Y.; Fang, C.; Li, T.; Liu, X.; Xia, Y.; Ye, F.; Zada, A.; Khan, M. Rational Design of Ti_3C_2/Carbon Nanotubes/$MnCo_2S_4$ Electrodes for Symmetric Supercapacitors with High Energy Storage. *Appl. Surf. Sci.* **2022**, *581*, No. 152432.

(24) Yu, L. P.; Zhou, X. H.; Lu, L.; Xu, L.; Wang, F. J. MXene/Carbon Nanotube Hybrids: Synthesis, Structures, Properties, and Applications. *ChemSusChem* **2021**, *14* (23), 5079−5111.

(25) Yan, P.; Zhang, R.; Jia, J.; Wu, C.; Zhou, A.; Xu, J.; Zhang, X. Enhanced Supercapacitive Performance of Delaminated Two-Dimensional Titanium Carbide/Carbon Nanotube Composites in Alkaline Electrolyte. *J. Power Sources* **2015**, *284*, 38−43.

(26) Yang, J.; Pan, Z.; Zhong, J.; Li, S.; Wang, J.; Chen, P.-Y. Electrostatic Self-Assembly of Heterostructured Black Phosphorus−MXene Nanocomposites for Flexible Microsupercapacitors with High Rate Performance. *Energy Storage Mater.* **2021**, *36*, 257−264.

(27) Liang, W.; Zhitomirsky, I. MXene−Carbon Nanotube Composite Electrodes for High Active Mass Asymmetric Supercapacitors. *J. Mater. Chem. A* **2021**, *9* (16), 10335−10344.

(28) Yang, L.; Zheng, W.; Zhang, P.; Chen, J.; Tian, W. B.; Zhang, Y. M.; Sun, Z. M. MXene/CNTs Films Prepared by Electrophoretic Deposition for Supercapacitor Electrodes. *J. Electroanal. Chem.* **2018**, *830*, 1−6.

(29) Thirumal, V.; Yuvakkumar, R.; Kumar, P. S.; Ravi, G.; Keerthana, S. P.; Velauthapillai, D. Facile Single-Step Synthesis of

MXene@CNTs Hybrid Nanocomposite by CVD Method to Remove Hazardous Pollutants. *Chemosphere* **2022**, *286*, No. 131733.
(30) Xiong, C.; Zhu, G. Y.; Jiang, H. R.; Chen, Q.; Zhao, T. S. Achieving Multiplexed Functionality in a Hierarchical MXene-Based Sulfur Host for High-Rate, High-Loading Lithium-Sulfur Batteries. *Energy Storage Mater.* **2020**, *33*, 147−157.
(31) Azami, M. S.; Jalil, A. A.; Hassan, N. S.; Hussain, I.; Fauzi, A. A.; Aziz, M. A. A. Green Carbonaceous Material−fibrous Silica-Titania Composite Photocatalysts for Enhanced Degradation of Toxic 2-Chlorophenol. *J. Hazard. Mater.* **2021**, *414*, No. 125524.
(32) Lv, L.; Guo, C.; Sun, W.; Wang, Y. Strong Surface-bound Sulfur in Carbon Nanotube Bridged Hierarchical Mo_2C-based MXene Nanosheets for Lithium−Sulfur Batteries. *Small* **2019**, *15* (3), No. 1804338.
(33) Luo, W.; Liu, Q.; Zhang, B.; Li, J.; Li, R.; Li, T.; Sun, Z.; Ma, Y. Binder-Free Flexible $Ti_3C_2T_x$ MXene/Reduced Graphene Oxide/Carbon Nanotubes Film as Electrode for Asymmetric Supercapacitor. *Chem. Eng. J.* **2023**, *474*, No. 145553.
(34) Zhang, Z.; Li, W.; Zhao, B.; Yang, X.; Zhao, C.; Wang, W.; Yang, X.; Shen, A.; Ye, M. Novel CNT/MXene Composite Membranes with Superior Electrocatalytic Efficiency and Durability for Sustainable Wastewater Treatment. *Chem. Eng. J.* **2024**, *495*, No. 153605.
(35) Li, S.; Zhang, Q.; Liu, L.; Wang, J.; Zhang, L.; Shi, M.; Chen, X. Ultra-Stable Sandwich Shaped Flexible MXene/CNT@Ni Films for High Performance Supercapacitor. *J. Alloys Compd.* **2023**, *941*, No. 168963.
(36) Jiang, K.; Li, Q.; Fan, S. Spinning Continuous Carbon Nanotube Yarns. *Nature* **2002**, *419*, 801.
(37) Jiang, K.; Wang, J.; Li, Q.; Liu, L.; Liu, C.; Fan, S. Superaligned Carbon Nanotube Arrays, Films, and Yarns: A Road to Applications. *Adv. Mater.* **2011**, *23* (9), 1154−1161.
(38) Luo, Y.; Wang, K.; Li, Q.; Fan, S.; Wang, J. Macroscopic Carbon Nanotube Structures for Lithium Batteries. *Small* **2020**, *16* (15), No. 1902719.
(39) Hong, Z.; Fang, Z.; Luo, Y.; Wu, H.; Tian, H.; Zhao, F.; Li, Q.; Fan, S.; Wang, J. Promising Nano-Silicon Anodes Prepared Using the "Disperse-Anchor" Strategy and Functional Carbon Nanotube Interlayers for Flexible Lithium-Ion Batteries. *J. Mater. Chem. A* **2022**, *10*, 23509−23520.
(40) Fang, Z.; Duan, S.; Liu, H.; Hong, Z.; Wu, H.; Zhao, F.; Li, Q.; Fan, S.; Duan, W.; Wang, J. Lithium Storage Mechanism and Application of Micron-Sized Lattice-Reversible Binary Intermetallic Compounds as High-Performance Flexible Lithium-Ion Battery Anodes. *Small* **2021**, *18*, No. 2105172.
(41) Liu, K.; Sun, Y.; Chen, L.; Feng, C.; Feng, X.; Jiang, K.; Zhao, Y.; Fan, S. Controlled Growth of Super-Aligned Carbon Nanotube Arrays for Spinning Continuous Unidirectional Sheets with Tunable Physical Properties. *Nano Lett.* **2008**, *8* (2), 700−705.
(42) Evans, J.; Vincent, C. A.; Bruce, P. G. Electrochemical Measurement of Transference Numbers in Polymer Electrolytes. *Polymer (Guildf).* **1987**, *28* (13), 2324−2328.
(43) Wang, X.; Cai, Y.; Wu, S.; Li, B. Sulfur Functions as the Activity Centers for High-Capacity Lithium Ion Batteries in S-and O-Bifunctionalized MXenes: A Density Functional Theory (DFT) Study. *Appl. Surf. Sci.* **2020**, *525*, No. 146501.
(44) Yu, X.; Yin, W.; Wang, T.; Zhang, Y. Decorating G-C_3N_4 Nanosheets with Ti_3C_2 MXene Nanoparticles for Efficient Oxygen Reduction Reaction. *Langmuir* **2019**, *35* (8), 2909−2916.
(45) Chen, X.; Li, J.; Pan, G.; Xu, W.; Zhu, J.; Zhou, D.; Li, D.; Chen, C.; Lu, G.; Song, H. Ti_3C_2 MXene Quantum Dots/TiO_2 Inverse Opal Heterojunction Electrode Platform for Superior Photoelectrochemical Biosensing. *Sensors Actuators B Chem.* **2019**, *289*, 131−137.
(46) Zhu, W.; Ye, F.; Li, M.; Wang, X.; Zhou, Q.; Fan, X.; Xue, J.; Li, X. In-Situ Growth of Wafer-like Ti_3C_2/Carbon Nanoparticle Hybrids with Excellent Tunable Electromagnetic Absorption Performance. *Compos. Part B Eng.* **2020**, *202*, No. 108408.
(47) Wang, H.; Zhao, R.; Hu, H.; Fan, X.; Zhang, D.; Wang, D. 0D/2D Heterojunctions of Ti_3C_2 MXene QDs/SiC as an Efficient and Robust Photocatalyst for Boosting the Visible Photocatalytic NO Pollutant Removal Ability. *ACS Appl. Mater. Interfaces* **2020**, *12* (36), 40176−40185.
(48) Cao, Y.; Zhang, Y.; Chen, H.; Qin, S.; Zhang, L.; Guo, S.; Yang, H. $Cu_{12}Sb_4S_{13}$ Quantum Dots/Few-Layered Ti_3C_2 Nanosheets with Enhanced K^+ Diffusion Dynamics for Efficient Potassium Ion Storage. *Adv. Funct. Mater.* **2022**, *32* (6), No. 2108574.
(49) Yang, B.; Liu, B.; Chen, J.; Ding, Y.; Sun, Y.; Tang, Y.; Yan, X. Realizing High-Performance Lithium Ion Hybrid Capacitor with a 3D MXene-Carbon Nanotube Composite Anode. *Chem. Eng. J.* **2022**, *429*, No. 132392.
(50) Zheng, W.; Zhang, P.; Chen, J.; Tian, W. B.; Zhang, Y. M.; Sun, Z. M. In Situ Synthesis of CNTs@Ti_3C_2 Hybrid Structures by Microwave Irradiation for High-Performance Anodes in Lithium Ion Batteries. *J. Mater. Chem. A* **2018**, *6* (8), 3543−3551.
(51) Rakhi, R. B.; Ahmed, B.; Hedhili, M. N.; Anjum, D. H.; Alshareef, H. N. Effect of Postetch Annealing Gas Composition on the Structural and Electrochemical Properties of Ti_2CT_x MXene Electrodes for Supercapacitor Applications. *Chem. Mater.* **2015**, *27* (15), 5314−5323.
(52) Wang, X.; Wang, S.; Qin, J.; Xie, X.; Yang, R.; Cao, M. Constructing Conductive Bridge Arrays between $Ti_3C_2T_x$ MXene Nanosheets for High-Performance Lithium-Ion Batteries and Highly Efficient Hydrogen Evolution. *Inorg. Chem.* **2019**, *58* (24), 16524−16536.
(53) Luo, S.; Patole, S.; Anwer, S.; Li, B.; Delclos, T.; Gogotsi, O.; Zahorodna, V.; Balitskyi, V.; Liao, K. Tensile Behaviors of $Ti_3C_2T_x$ (MXene) Films. *Nanotechnology* **2020**, *31* (39), 395704.
(54) Zhang, M.; Liang, R.; Yang, N.; Gao, R.; Zheng, Y.; Deng, Y.; Hu, Y.; Yu, A.; Chen, Z. Eutectic Etching toward In-Plane Porosity Manipulation of Cl-Terminated MXene for High-Performance Dual-Ion Battery Anode. *Adv. Energy Mater.* **2022**, *12* (1), No. 2102493.
(55) Mashtalir, O.; Lukatskaya, M. R.; Zhao, M. Q.; Barsoum, M. W.; Gogotsi, Y. Amine-Assisted Delamination of Nb_2C MXene for Li-Ion Energy Storage Devices. *Adv. Mater.* **2015**, *27* (23), 3501−3506.
(56) Li, Y.; Arnold, S.; Husmann, S.; Presser, V. Recycling and Second Life of MXene Electrodes for Lithium-Ion Batteries and Sodium-Ion Batteries. *J. Energy Storage* **2023**, *60*, No. 106625.
(57) Wang, Z.; Duan, C.; Zhou, Y.; Wen, F.; Lu, Q.; Liu, D.; Wang, F.; Meng, X. Ag Decorated 3D Honeycomb-like MXene Architecture as an Advanced Lithium-Ion Anode Material towards High Capacity and Long-Term Cycle Capability. *Appl. Surf. Sci.* **2023**, *615*, No. 156406.
(58) Collins, G. A.; Geaney, H.; Ryan, K. M. Alternative Anodes for Low Temperature Lithium-Ion Batteries. *J. Mater. Chem. A* **2021**, *9* (25), 14172−14213.
(59) Wang, J.; Polleux, J.; Lim, J.; Dunn, B. Pseudocapacitive Contributions to Electrochemical Energy Storage in TiO_2 (Anatase) Nanoparticles. *J. Phys. Chem. C* **2007**, *111* (40), 14925−14931.

https://doi.org/10.1021/acsaem.4c01650
ACS Appl. Energy Mater. 2024, 7, 8004−8013